Dispersion and lifetime of the SO_2 cloud from the August 2008 Kasatochi eruption

N. A. Krotkov,[1] M. R. Schoeberl,[2] G. A. Morris,[3] S. Carn,[4] and K. Yang[5]

Received 1 February 2010; revised 23 September 2010; accepted 29 September 2010; published 21 December 2010.

[1] Hemispherical dispersion of the SO_2 cloud from the August 2008 Kasatochi eruption is analyzed using satellite data from the Ozone Monitoring Instrument (OMI) and the Goddard Trajectory Model (GTM). The operational OMI retrievals underestimate the total SO_2 mass by 20–30% on 8–11 August, as compared with more accurate offline Extended Iterative Spectral Fit (EISF) retrievals, but the error decreases with time due to plume dispersion and a drop in peak SO_2 column densities. The GTM runs were initialized with and compared to the operational OMI SO_2 data during early plume dispersion to constrain SO_2 plume heights and eruption times. The most probable SO_2 heights during initial dispersion are estimated to be 10–12 km, in agreement with direct height retrievals using EISF algorithm and IR measurements. Using these height constraints a forward GTM run was initialized on 11 August to compare with the month-long Kasatochi SO_2 cloud dispersion patterns. Predicted volcanic cloud locations generally agree with OMI observations, although some discrepancies were observed. Operational OMI SO_2 burdens were refined using GTM-predicted mass-weighted probability density height distributions. The total refined SO_2 mass was integrated over the Northern Hemisphere to place empirical constraints on the SO_2 chemical decay rate. The resulting lower limit of the Kasatochi SO_2 e-folding time is ~8–9 days. Extrapolation of the exponential decay back in time yields an initial erupted SO_2 mass of ~2.2 Tg on 8 August, twice as much as the measured mass on that day.

Citation: Krotkov, N. A., M. R. Schoeberl, G. A. Morris, S. Carn, and K. Yang (2010), Dispersion and lifetime of the SO_2 cloud from the August 2008 Kasatochi eruption, *J. Geophys. Res.*, *115*, D00L20, doi:10.1029/2010JD013984.

1. Introduction

[2] Kasatochi Volcano (52.18°N, 175.51°W) is one of many mostly submarine volcanoes whose summit emerges from the waters of the Bering Sea off the southwest coast of Alaska. After short precursory seismic activity starting on 7 August, Kasatochi erupted several times injecting sulfur dioxide (SO_2) and ash directly into the Arctic lower stratosphere [*Dean et al.*, 2008; *Waythomas et al.*, 2010]. Satellite measurements of the SO_2 loading by ultraviolet (UV) and infrared (IR) sensors found a maximum total SO_2 mass of ~0.5–2.7 Tg in the Kasatochi volcanic cloud [*Richter et al.*, 2009; *Corradini et al.*, 2010; *Karagulian et al.*, 2010; *Kristiansen et al.*, 2010; *Prata et al.*, 2010; *Yang et al.*, 2010]. Emission of ~2–3 Tg SO_2 ranks the 2008 Kasatochi eruption as the largest SO_2 release measured since the August 1991 eruption of Cerro Hudson (Chile), and the largest at high northern latitudes since the beginning of space-based SO_2 measurements in 1978 [*Carn et al.*, 2003].

[3] Compared to volcanic ash clouds that have atmospheric residence times of a few days, the lifetime of volcanic SO_2 in the upper troposphere and lower stratosphere (UTLS) is typically longer [*Bluth et al.*, 1992; *Guo et al.*, 2004; *Prata and Bernardo*, 2007; *Eckhardt et al.*, 2008], allowing for the monitoring of plume dispersion for extended time periods. The main mechanism of removal of stratospheric SO_2 is photochemical conversion to sulfuric acid though gas-phase reaction with the hydroxyl radical, OH [*McKeen et al.*, 1984; *Chin et al.*, 1996, 2000; *Koch et al.*, 1999; *Barth et al.*, 2000]. Sulfuric acid is hygroscopic and subsequently forms sulfate aerosol with stratospheric residence times from months to years [*Junge et al.*, 1961; *Rosen*, 1971]. Sulfate aerosol plays an important role in climate change and atmospheric chemistry [e.g., *Robock*, 2000]. By scattering and absorbing solar and terrestrial radiation, they cause a direct radiative forcing of climate. Sulfate particles also influence the microphysics of meteorological clouds formed in their presence, resulting in indirect aerosol effects (e.g., impacts on the reflectivity of clouds) [*Twomey*, 1977]. By providing the surface for heterogeneous chemical reactions that liberate chlorine,

[1]NASA Goddard Space Flight Center, Greenbelt, Maryland, USA.
[2]Science and Technology Corporation, Columbia, Maryland, USA.
[3]Department of Physics and Astronomy, Valparaiso University, Valparaiso, Indiana, USA.
[4]Department of Geological and Mining Engineering and Sciences, Michigan Technological University, Houghton, Michigan, USA.
[5]Goddard Earth Sciences and Technology Center, University of Maryland Baltimore County, Baltimore, Maryland, USA.

0148-0227/10/2010JD013984

volcanogenic sulfate aerosol can promote depletion of stratospheric O_3 [*Russell et al.*, 1996; *Solomon*, 1999]. *Intergovernmental Panel on Climate Change* [2007] stresses a low level of scientific understanding of the direct radiative forcing of volcanic sulfate particles, primarily due to a lack of knowledge of the spatiotemporal variability of this forcing. Accurate quantification of stratospheric SO_2 injections by volcanic eruptions is also critical input to the debate over geoengineering proposals to modify climate by stratospheric injection of sulfate aerosol precursors [e.g., *Crutzen*, 2006; *Wigley*, 2006; *Robock et al.*, 2008].

[4] The residence time of volcanic sulfate aerosol and its cooling effect on climate depend on SO_2 injection height, total mass and dispersion pattern. Daily satellite retrievals of SO_2 column densities in the North Pacific region are currently provided by several polar-orbiting sensors, including the Infrared Atmospheric Sounding Interferometer (IASI) [*Karagulian et al.*, 2010] and UV Global Ozone Monitoring Experiment-2 (GOME-2) [*Richter et al.*, 2009], both on the MetOp-A satellite, the UV Ozone Monitoring Instrument (OMI) on NASA's Aura satellite [*Krotkov et al.*, 2006; *Yang et al.*, 2007, 2010], the UV Scanning Imaging Absorption Spectrometer for Atmospheric Cartography (SCIAMACHY) instrument on ENVISAT [*Bovensmann et al.*, 1999; *Lee et al.*, 2008], the Atmospheric Infrared Sounder (AIRS) on NASA's Aqua spacecraft [*Prata and Bernardo*, 2007], and the Moderate Resolution Imaging Spectroradiometer (MODIS) on the Terra and Aqua satellites [*Watson et al.*, 2004; *Corradini et al.*, 2010]. Measurements from multiple platforms with different overpass times, using different spectral regions, permit intercomparisons between retrievals, and more accurate estimates of volcanic SO_2 emissions and their temporal evolution. It should be noted however, that satellite retrievals of volcanic SO_2 remain largely unvalidated, although some validation of OMI SO_2 data was achieved after the 2008 eruption of Okmok volcano (Aleutian Islands) [*Spinei et al.*, 2010].

[5] UV data from OMI and GOME-2, and SO_2 retrievals using the 8.6 μm MODIS band, yield the highest estimates of SO_2 loading by the Kasatochi eruption (~2–3 Tg) [*Richter et al.*, 2009; *Corradini et al.*, 2010; *Yang et al.*, 2010], perhaps due to increased sensitivity to the lower troposphere at these wavelengths. Several approaches have also been used to estimate the altitude of the Kasatochi SO_2 cloud from satellite data, with some convergence of results. Independent estimates from inversion of UV and IR radiances indicate altitudes of ~9–11 km [*Yang et al.*, 2010] and 12.5 ± 4 km [*Karagulian et al.*, 2010], and inverse trajectory modeling using assimilated SO_2 data from GOME-2, OMI and AIRS yields an emission maximum at ~12 km [*Kristiansen et al.*, 2010]. These estimates are in good agreement with direct measurements of aerosol altitude by the spaceborne CALIPSO lidar [*Yang et al.*, 2010]. In the weeks and months following the Kasatochi eruption, sulfate aerosol absorption was detected in IR IASI spectra [*Karagulian et al.*, 2010] and the evolution of the stratospheric aerosol enhancement was followed using satellite limb sounders [*Bourassa et al.*, 2010; *Sioris et al.*, 2010]. *Karagulian et al.* [2010] estimate an e-folding time for SO_2 loss of 18 days based on IASI data.

[6] In this paper we analyze the month-long Kasatochi SO_2 cloud dispersion, height and chemical mass decay using UV measurements from OMI and trajectory modeling [*Schoeberl and Sparling*, 1995]. OMI is a Dutch-Finnish hyperspectral UV spectrometer [*Levelt et al.*, 2006] launched in 2004 on board Aura [*Schoeberl et al.*, 2006]. Compared to concurrent UV and IR satellite sensors [*Prata et al.*, 2003; *Carn et al.*, 2005; *Richter et al.*, 2006; *Prata and Bernardo*, 2007; *Prata and Kerkmann*, 2007; *Clerbaux et al.*, 2008; *Lee et al.*, 2008; *Clarisse et al.*, 2008; *Richter et al.*, 2009] OMI offers a combination of high sensitivity to total column SO_2, the best spatial resolution in the UV (13 × 24 km at nadir) and contiguous daily global coverage [*Levelt et al.*, 2006]. The OMI UTLS SO_2 noise is ~0.3 DU (1 standard deviation, σ, 1 Dobson Unit [DU] = $2.69 \cdot 10^{16}$ molecules/cm^2) [*Krotkov et al.*, 2006; *Yang et al.*, 2007]. The OMI detection limit, determined as 5 adjacent pixels with SO_2 columns larger than 5σ, is 30–50 tons, is smaller by a factor of 200 compared to the Total Ozone Mapping Spectrometer (TOMS) [*Heath et al.*, 1975; *Krueger et al.*, 1995, 2000, 2009a; *Carn et al.*, 2003] (http://so2.umbc.edu/). Assuming a similar noise level, the OMI detection limit is 20–30 times smaller than that for the GOME-2 instrument [*Krueger et al.*, 2009a] and ~10 times smaller than SCIAMACHY [*Bovensmann et al.*, 1999; *Richter et al.*, 2006]. The improved sensitivity and smaller footprint of OMI have extended the range of satellite SO_2 detection to degassing volcanoes [*Carn et al.*, 2008, 2009], older volcanic clouds, and to large anthropogenic pollution [*Krotkov et al.*, 2006, 2008; *Carn et al.*, 2007]. The small OMI SO_2 detection limit is especially useful for the hemispherical tracking of the Kasatochi SO_2 cloud, allowing for more accurate estimates of SO_2 to sulfate conversion rate.

[7] As with other satellite sensors, the accuracy of the OMI SO_2 mass retrievals depends not just on noise, but also on the retrieval algorithm applied to the measured radiances and ultimately on the validity of the forward model and a priori assumptions. The most important a priori assumption is SO_2 height (i.e., center of mass altitude, CMA [*Krotkov et al.*, 2008]). The CMA can be estimated either from independent measurements (e.g., satellite or ground-based) or by comparing satellite SO_2 maps with trajectory models. In this paper we explore both approaches. In section 2 we compare OMI retrievals of SO_2 burdens and heights using an advanced algorithm [*Yang et al.*, 2010] with the operational data. The use of the Goddard Trajectory Model (GTM) [*Schoeberl and Sparling*, 1995] in conjunction with OMI operational data is discussed in section 3. The GTM is initialized with OMI observations on 10 August using a variety of cloud altitudes. By comparing observed and forecast positions on the next day, probable altitudes are selected. In the second scheme trajectories from multiple altitudes starting on 10 August are run backward. By selecting trajectories originating near the volcano, the altitudes and eruption times are confirmed. Finally, the GTM is reinitialized using observed positions and estimated altitudes on 11 August and run forward to compare the forecast dispersion patterns with OMI observations and estimate probable SO_2 heights through the end of August. In section 4, operational SO_2 data are refined to obtain a "best estimate" of daily mass using GTM-estimated SO_2 heights. Refined OMI daily SO_2 burdens and dispersion

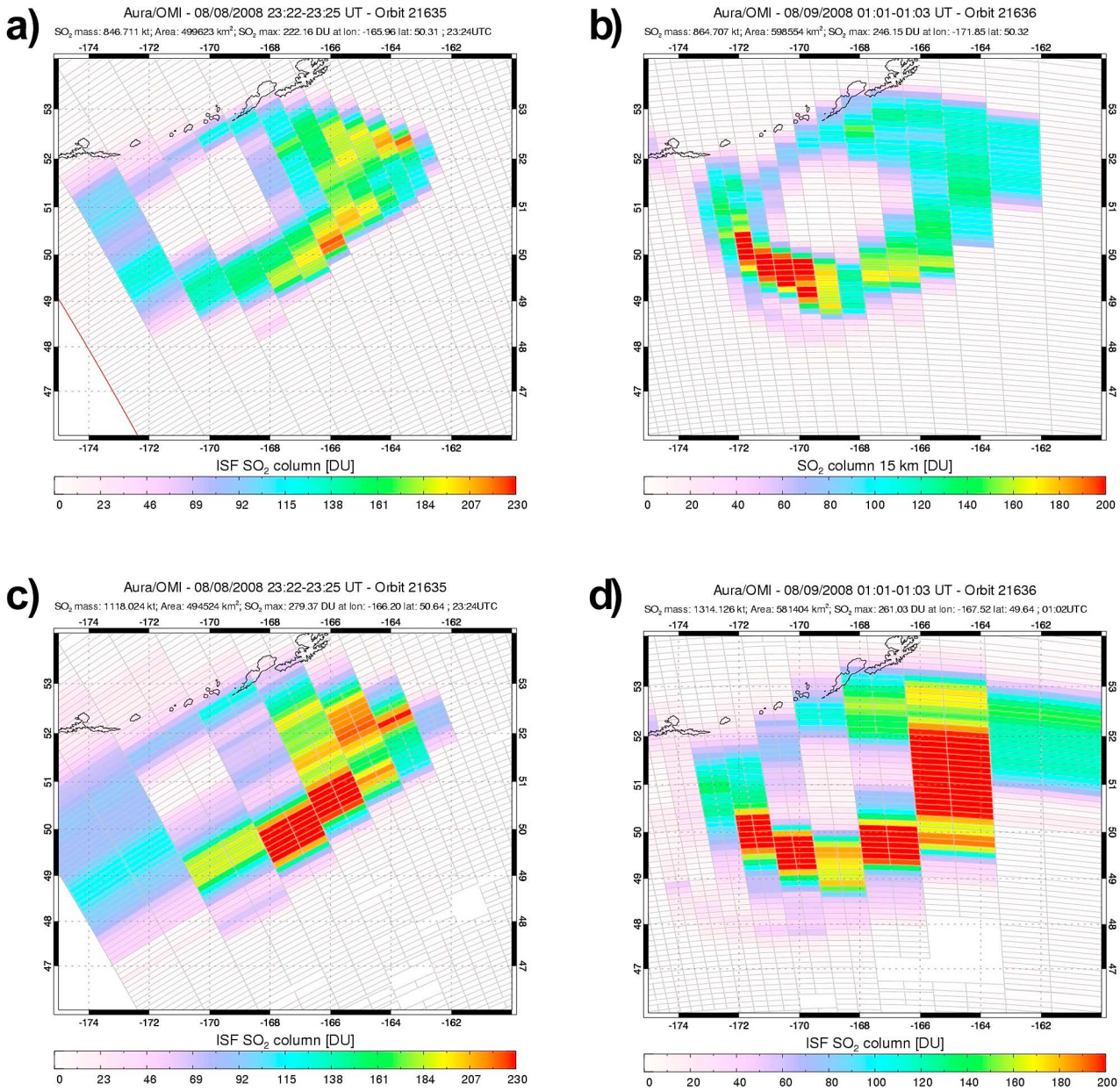

Figure 1. Operational OMI STL SO_2 data (a) on 8 August at 2323 UT (orbit 21635) and (b) during the next overpass on 9 August at 0102 UT (orbit 21636). The SO_2 mass calculation yields ~0.85–0.86 Tg assuming a plume height between 15 and 20 km and ~1 Tg assuming a plume height between 5 and 10 km. Although the overall shape, mass, and area of the plume has not changed significantly between the two orbits, the spatial distribution of SO_2 is affected by the increasing the OMI footprint for off-nadir viewing directions. OMI off-line EISF retrievals for the same orbit as (c) Figure 1a and (d) Figure 1b [*Yang et al.*, 2010]. The EISF SO_2 mass is ~1.1–1.3 Tg, which is ~30% larger than the operational data.

areas are used to constrain the Kasatochi SO_2 chemical decay rate.

2. OMI SO_2 Observations

[8] OMI makes measurements of ozone and SO_2 absorption in the middle UV spectral region, from which total column SO_2 and ozone amounts are derived. OMI sensitivity is roughly constant throughout the stratosphere, but decreases throughout the troposphere. OMI data are operationally processed with the fast Linear Fit (LF) algorithm [*Yang et al.*, 2007] assuming a priori SO_2 and ozone vertical profiles. Volcanic data samples can be reprocessed using an advanced extended iterative spectral fit (EISF) algorithm, allowing simultaneous retrievals of SO_2 loading and height [*Yang et al.*, 2010]. We briefly describe both algorithms and compare SO_2 mass calculations for the first 2 days following the Kasatochi eruption.

2.1. OMI SO_2 Retrievals

[9] Operational OMI SO_2 data are processed in near real time (NRT) using the fast LF algorithm and predicted orbital parameters. Global and regional SO_2 images are automatically generated by NOAA/NESDIS and are typically available within 3 h of the Aura overpass at the Web site: http://satepsanone.nesdis.noaa.gov/pub/OMI/OMISO2/index.html [*Krueger et al.*, 2009b]. The science quality operational data are reprocessed within a day and archived at NASA's Goddard Space Flight Center Earth Sciences (GES) Data and Information Services Center at http://disc.sci.gsfc.nasa.gov/Aura/data-holdings/OMI/omso2g_v003.shtml. The LF algorithm uses the TOMS–like total ozone retrieval (OMTO3) (P. K. Bhartia and C. W. Wellemeyer, OMI TOMS-V8 total O_3 algorithm, 2002, http://eospso.gsfc.nasa.gov/eos_homepage/for_scientists/atbd/docs/OMI/ATBD-OMI-02.pdf) as a linearization step to derive an initial estimate of total ozone (assuming zero SO_2) and the effective cloud fraction. The radiance residuals at the 10 wavelengths (i.e., vacuum wavelengths 308.7 nm, 310.8 nm, 311.85 nm, 312.61 nm, 313.2 nm, 314.4 nm, 322.42 nm, 345.4 nm, 360.15 nm, 375 nm) are calculated as the difference between the measured and computed N values ($N = -100*\log_{10}(I/F)$; I is Earth radiance and F is solar irradiance) using a vector forward model radiative transfer code, that accounts for multiple Rayleigh scattering, ozone absorption, Ring effect, and surface reflectivity [*Dave*, 1964]. Cloudy scenes are treated as mixture of two opaque Lambertian surfaces (Modified Lambertian Reflectivity Model (MLER) [*Ahmad et al.*, 2004]), one at the terrain pressure and the other at the Radiative Cloud Pressure (RCP) derived using OMI-measured Rotational Raman scattering at around 350 nm [*Joiner and Vasilkov*, 2006]. In the presence of SO_2, the residuals contain spectral structures that correlate with the SO_2 absorption cross section. The residuals also have contributions from other error sources that have not yet been identified. To reduce interference from other error sources a median residual for a sliding group of SO_2-free and cloud-free scenes (radiative cloud fraction <0.15) covering ±15° latitude along the orbit track is subtracted from each spectral band and cross-track position, thereby reducing cross-track and latitudinal biases. The LF algorithm is optimized to derive SO_2 produced by large volcanic eruptions in NRT. It minimizes different subsets of the residuals by simultaneously adjusting total SO_2, ozone, and the coefficients of a quadratic polynomial parameterization of the effective scene reflectivity. The subsets are determined by the process of dropping the shortest (and most SO_2 sensitive) wavelength bands one at a time until the 322 nm band is reached. The largest SO_2 retrieval is reported as the final estimate. This still can be an underestimate for SO_2 column amounts larger than ~100 DU [*Yang et al.*, 2009]. The assumed gaseous vertical profiles correspond to the standard OMTO3 ozone profiles defined in Umkehr pressure layers (~5 km thick). The three reported volcanic SO_2 columns assume SO_2 localized in Umkehr layers 0, 1 and 3 for lower tropospheric (TRL), midtropospheric (TRM), and lower stratospheric (STL) SO_2 clouds, respectively. In the Kasatochi case we interpolate between the operational STL and TRM SO_2 columns with corresponding CMAs of ~17 km and ~7 km.

[10] The Iterative Spectral Fit (ISF) algorithm simultaneously fits all OMI hyperspectral measurements in the UV2 wavelength range between ~310 nm and 345 nm using prescribed OMTO3 ozone and SO_2 profiles [*Yang et al.*, 2009]. The forward model is similar to the LF algorithm, but without a sliding median residual correction. The important difference is that the ISF algorithm updates residuals and weighting functions in an iterative process allowing retrieval of larger SO_2 columns up to ~1000 DU. Assigning an a priori SO2 vertical profile shape is a source of systematic error. The Extended Iterative Spectral Fit (EISF) algorithm derives the SO_2 plume height in addition to the SO_2 column by simultaneously fitting OMI hyperspectral measurements in both UV2 (310–345 nm) and the shorter wavelength UV1 spectral regions [*Yang et al.*, 2010]. Thus, the EISF algorithm takes advantage of the larger number of hyperspectral UV measurements to provide higher-precision retrievals and new information on SO_2 height, but is more demanding for processing resources and cannot currently be used in operational processing. Since EISF retrievals utilize both UV1 and UV2 (lower spatial resolution) OMI spectral detectors, coadding of UV2 spatial pixels is required [*Levelt et al.*, 2006], which results in degraded spatial resolution (Figure 1).

2.2. OMI SO_2 Observations of Early Kasatochi Cloud Dispersion

[11] Table 1 presents a summary of all OMI observations of the Kasatochi SO_2 cloud in August 2008. Operational SO2 burdens are interpolated between STL (CMA = ~17 km) and TRM vertical profiles (CMA = ~7 km) assuming model estimated CMA (Table 2). OMI first captured the Kasatochi SO_2 plume in two consecutive overpasses on 8 August prior to the major explosive eruption between 0400 and 0500 UT (the early overpass at ~0020 UT is included in the 7 August daily file, while the next overpass at ~0200 UT is included in the 8 August daily file; see Table 1). The relatively small SO_2 mass detected on these two early overpasses suggests that the eruption cloud was still developing at this stage. Figure 1 shows SO_2 retrievals during the next consecutive OMI overpasses over Kasatochi on 8 August at ~2323 UT and early on 9 August at ~0102 UT. The SO_2 cloud resulted from the strongest Kasatochi eruption on 8 August at ~0400–0500 UT. After ~19 h of dispersion the cloud was embedded in a rotating weather system that caused it to wrap around into a ring shape. In both overpasses (1.5 h apart) OMI data show maximum SO_2 columns of over 200 DU with a ~30% operational mass underestimation (operational mass of ~0.85–1 Tg compared to EISF mass of ~1.1–1.3 Tg). This underestimation is consistent with high SO_2 loadings and possible interference from high ash loadings [*Yang et al.*, 2010].

[12] At 2223 UT on 9 August, OMI captured the eastern part of the plume over the Gulf of Alaska at 48°N–50°N and 160°W with an operational SO_2 mass of ~0.46 Tg. On the next overpass at ~0005 UT on 10 August, OMI captured the whole cloud in a single orbit for the last time, with a peak SO_2 column exceeding 270 DU, and an operational SO_2 mass of ~1.3 Tg (a ~15% underestimation compared to the EISF mass of ~1.5 Tg) covering an area of ~10^6 km^2 (Table 1). This makes the Kasatochi eruption the largest SO_2 release since the Pinatubo and Cerro Hudson eruptions in

Table 1. OMI SO_2 Observations for the August 2008 Mount Kasatochi Eruption

Date[a]	Orbits and Time (UT)	Max STL SO_2 and (Max EISF) (DU)	Mean STL SO_2 and (StDev) (DU)	GTM Height and (EISF[b]) (km)	SO_2 Mass: Operational[c] and (EISF[b]) (Tg)
5 Aug	o21579–o21593	3	0.004 (0.22)	N/A	0.01
6 Aug	o21594–o21606	8	0.003 (0.21)	N/A	0.02
7 Aug	o21607–o21621	25	−0.005 (0.22)	N/A	0.001
8 Aug	o21635 (2322–2325)	222 (279)	N/A	10.8	0.85 (1.1)
9 Aug	o21636 (0101–0103)	246 (261)	N/A	10.7 (10.5)	0.87 (1.3)
10 Aug	o21650 (0004–0007)	271 (280)	N/A	10.7 (10.5)	1.34 (1.6)
10 Aug	o21663 + o21664 (2130–2314)	236 (208)	N/A	10.6 (10.3)	1.55 (1.8)
11 Aug	o21665–o21679	190	0.40 (4.1)	10.5	1.4 (1. 6)
12 Aug	o21680–o21694	166	0.33 (3.0)	10.4	1.34
13 Aug	o21695–o21708	145	0.39 (3.1)	10.3	1.20
14 Aug	o21709–o21724	67	0.34 (2.0)	10.3	1.30
15 Aug	o21724–o21737	58	0.29 (1.6)	10.3	1.11
16 Aug	o21739–o21752	49	0.25 (1.2)	10.1	1.02
17 Aug	o21753–o21767	41	0.22 (1.0)	10.0	0.85
18 Aug	o21768–o21781	33	0.21 (0.9)	9.7	0.78
19 Aug	o21783–o21796		0.17 (1.0)	9.5	0.65
20 Aug	o21797–o21810	22	0.17 (0.6)	9.3	0.55
21 Aug	o21811–o21825	9	0.16 (0.6)	9.1	0.53
22 Aug	o21826–o21839	14	0.14 (0.5)	8.9	0.47
23 Aug	o21840–o21854		0.11 (0.7)	8.7	0.38
26 Aug	o21884–o21898	26	0.08 (0.4)	8.2	0.30
27 Aug	o21899–o21912	12	0.08 (0.3)	8.0	0.30
29 Aug	o21928–o21941	5	0.06 (0.3)	7.8	0.26
30 Aug	o21942–o21956	5	0.05 (0.3)	7.6	0.20
31 Aug	o21957–o21970	4	0.04 (0.3)	7.5	0.18
1 Sep	o21971–o21985	6	0.04 (0.3)	7.4	0.19
2 Sep	o21986–o22000		0.04 (0.6)	7.2	0.17
3 Sep	o22001–o22014	3	0.04 (0.2)	7.0	0.18
4 Sep	o22015–o22029	9	0.03 (0.2)	6.9	0.15
5 Sep	o22030–o22043	13	0.04 (0.2)	6.8	0.15
6 Sep	o22044–o22058	7	0.03 (0.2)	6.6	0.14
7 Sep	o22059–o22072	12	0.03 (0.2)	6.5	0.13
8 Sep	o22073–o22087	13	0.03 (0.4)	6.3	0.12
9 Sep	o22088–o22101	5	0.02 (0.2)	6.2	0.08
10 Sep	o22102–o22116	5	0.02 (0.2)	6.0	0.11

[a]OMI date is based on equator crossing UT time.
[b]SO_2 Mass and effective height calculation using off-line EISF retrievals [*Yang et al.*, 2010].
[c]Total mass calculation using all OMI pixels in a region including volcanic cloud (for individual orbits) on 8–10 August. On 11 August to 10 September summing masses for all grid cells in Northern Hemisphere (~1.5×10^6 grid cells between 30°N and 90°N).

1991 and the largest at high northern latitudes since satellite observations of SO_2 began in 1978. Later on 10 August, the cloud continued drifting eastward over the Gulf of Alaska while rotating counterclockwise. The eastern part of the cloud was caught in the jet stream, resulting in rapid advection eastward. By the end of the day the leading edge of the cloud had reached the West Coast of Canada (Figure 2). Just after reaching the coast the cloud split into northern and southern branches due to wind shear. The higher part of the cloud followed the southern branch, traveling southeast toward the Canada–United States border, while the lower part followed the northern branch, moving over the Yukon Territory, Canada, and reaching high latitudes ~65°N at 2200 UT. The core of the plume, which contained most of the SO_2 columns above 200 DU, drifted more slowly over the Gulf of Alaska eastward toward the United States and Canada (Figure 2). The operational SO_2 mass on 10 August was ~1.3–1.5 Tg, which is slightly larger than measured on 9 August (Table 1), but comparable to the differences between the OMI algorithms (EISF mass was ~1.5–1.8 Tg on 10 August, which is ~15% higher than the EISF mass on 9 August; see Table 1). The area of the plume increased from just ~$0.6 \cdot 10^6$ km^2 on 8–9 August (see Figure 1) to >$2 \cdot 10^6$ km^2 between the early and late overpasses on 10 August (see Figure 2). Dispersion of the plume decreases the peak column SO_2 amounts, leading to better UV penetration and a more accurate mass estimation. By comparing operational and EISF retrievals we estimate that operational OMI data underestimate the total SO_2 mass by 20% on 10 August. We assume that the underestimation in the operational SO_2 mass decreases on the following days

Table 2. Mean, Standard Deviation, and Most Probable Altitudes for the Distribution of Parcels in the Kinematic GTM as a Function of Time[a]

Date	Mean z (km)	σ z (km)	Most Probable z (km)
080811	10.5	3.2	10.25
080813	10.3	3.2	10.25
080815	10.3	3.2	10.25
080817	10.0	3.2	10.25
080819	9.5	3.1	10.25
080821	9.1	3.0	9.75
080823	8.7	3.0	9.75
080825	8.5	2.9	9.75
080827	8.0	2.8	9.75
080829	7.8	2.8	9.75
080831	7.5	2.7	9.75

[a]See text for details. Date given as yymmdd.

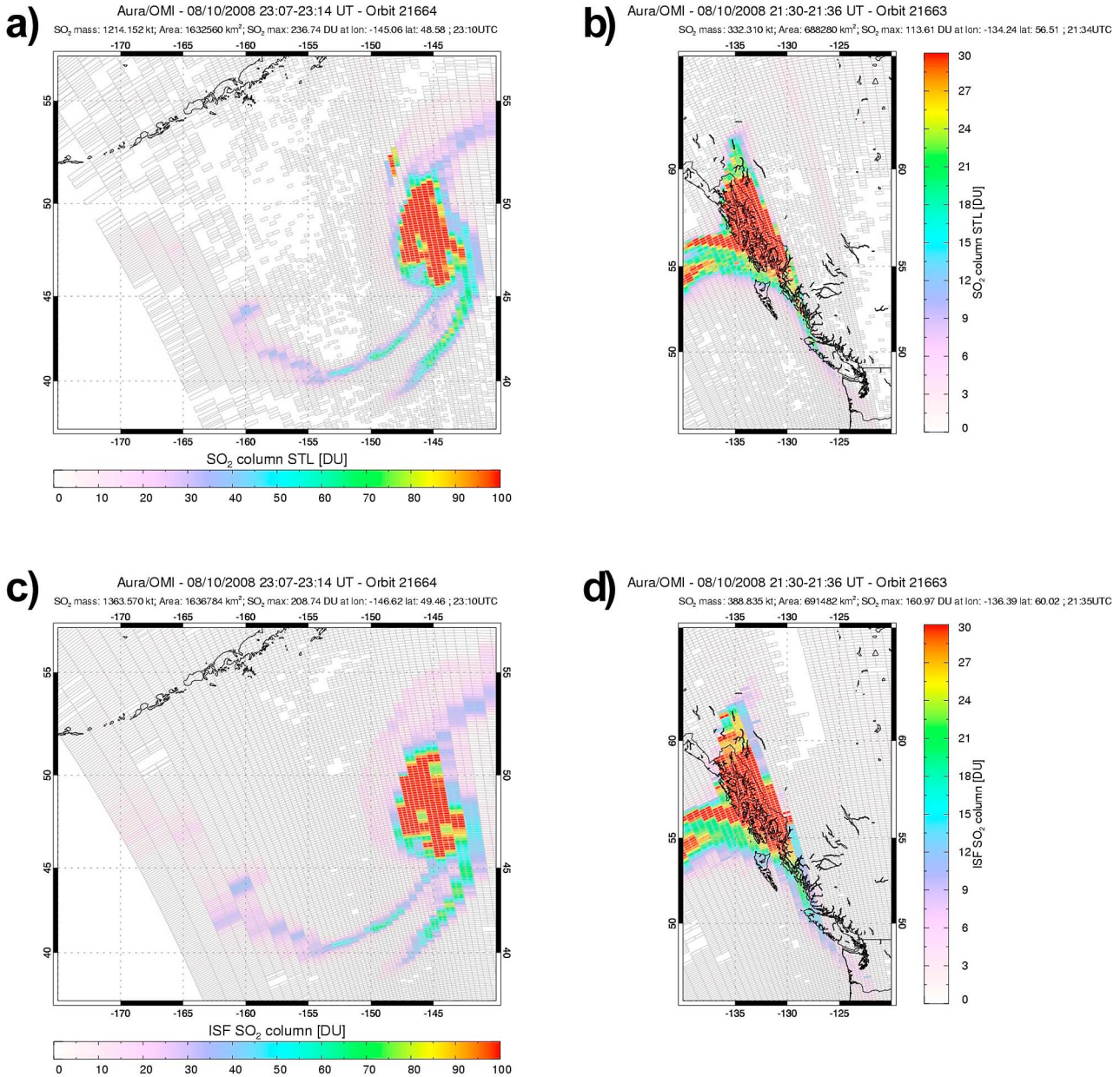

Figure 2. Same as Figure 1 but on 10 August: OMI view of Kasatochi cloud (a and c) at 2306 UT from orbit 21664 and (b and d) at 2135 UT from orbit 21663: operational LF retrievals (Figures 2a and 2b) and off-line EISF retrievals [*Yang et al.*, 2010] (Figures 2c and 2d). The operational mass (combined orbits 21663 and 21664) is ~1.55 Tg, which is 13% smaller than the EISF mass 1.75 Tg.

due to plume dispersion and a drop in peak SO_2 column densities. We therefore compare the SO_2 dispersion patterns with trajectory model using operational STL retrievals that have the lowest background noise (<0.3 DU).

3. Trajectory Modeling of Kasatochi SO_2 Cloud Dispersion

3.1. Trajectory Model

[13] All Lagrangian dispersion models (e.g., HYSPLIT, R. R. Draxler and G. D. Rolph, 2010, http://ready.arl.noaa.gov/HYSPLIT.php), FLEXPART [*Stohl et al.*, 1998]) use the same underlying physic and if they meet a few basic tests (e.g., to run the particle forward and then backward to see if it arrives at the initial location) they all get the same results. The differences might be in the meteorological fields used or other details. We use the Goddard Trajectory Model (GTM) [*Schoeberl and Sparling*, 1995], which has both diabatic (advection on isentropes) and kinematic (advection on isobars) versions. *Schoeberl et al.* [1993] and *Allen and Schoeberl* [1999] demonstrated the use of the GTM for tracking volcanic plumes. However, since those papers were published, global meteorological analyses and Lagrangian dispersion models have significantly improved allowing one to use the trajectory calculations to obtain additional information on the plume altitude [*Prata et al.*, 2007; *Eckhardt*

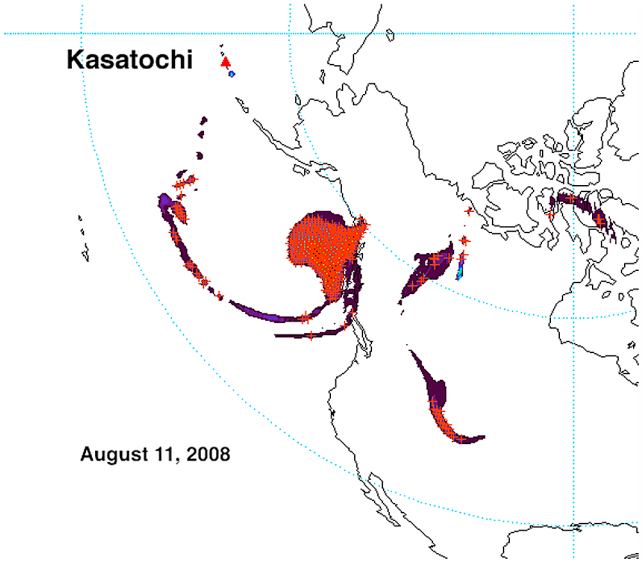

Figure 3. SO_2 column observations from OMI on 11 August 2008 (purple shades) and the trajectory points (red crosses). Red triangle is the location of Kasatochi Island. The data are binned into 1/2 degree latitude-longitude boxes. These trajectory points have been selected from the initial ensemble because they line up with the SO_2 plume where SO_2 > 5 DU.

et al., 2008; *Kristiansen et al.*, 2010]. Here the GTM uses the latest NASA Goddard Earth Observing System (GEOS-5) winds and temperatures (http://gmao.gsfc.nasa.gov/systems/geos5/) that are similar to the meteorological analysis fields provided by the European Centre for Medium-Range Weather Forecasts (ECMWF; http://www.ecmwf.int/) that drive the FLEXPART model [*Kristiansen et al.*, 2010].

[14] The winds and temperatures are interpolated on to parcel positions and the parcels are advected forward or backward using the horizontal and vertical velocities (in the kinematic version) from the model. The numerical method is a fourth-order Runge-Kutta advection scheme, applied using time and space interpolated wind and temperature fields from the analysis. Generally speaking individual trajectories are valid for about a week before the accumulated error becomes a problem. Additional errors might occur where the wind analysis is bad or where the ash cloud is heated by sunlight or surface IR and that heating can create a small amount of vertical motion not included in the meteorological model. This latter effect appears small over the period of integration since the trajectory model tracks the cloud fairly accurately without including additional volcanic cloud heating. Other volcanic trajectory simulations we have performed (Pinatubo, St. Helens, Mount Hudson, Soufriere Hills) have also not required the inclusion of ash cloud heating.

3.2. Forward Trajectory Analysis of the Kasatochi Eruption Cloud

[15] Parcels are initialized in an isentropic version of the GTM at the times and locations of each of the OMI SO_2 measurements on early overpass on 10 August between the potential temperature levels 330 K (~5.5 km) and 355 K (~13.6 km). The range of altitudes was chosen from an initial assessment using a much wider range of altitudes extending from 2–20 km. Parcels outside the range 5.5–13.6 km did not match subsequent SO_2 observations. The GTM moves the parcels forward adiabatically to the next day's observation times. Their positions are then compared to the SO_2 measurements made by OMI on 11 August. Figure 3 shows the OMI SO_2 observations for 11 August regridded onto a 1/2 degree latitude-longitude array together with retained Kasatochi GTM parcels. Because we do not know the altitude distribution of the plume, we compared high SO_2 column regions on 11 August with concentrations of trajectory parcels. We select bins (grid cells) where the OMI STL SO_2 > 5 DU and there are at least five trajectory parcels in a bin. Figure 3 shows the subsequent map of SO_2 and trajectory parcels meeting these criteria. This screening approach generates an ensemble of parcels most likely corresponding to the altitude distribution of the plume (Figure 4).

[16] We now use this distribution of parcels to initialize a kinematic version of the GTM to run forward in time from 11 to 31 August. We use the kinematic rather than isentropic version to examine the long-term dispersion of the volcanic cloud since isentropic trajectory calculations degrade after

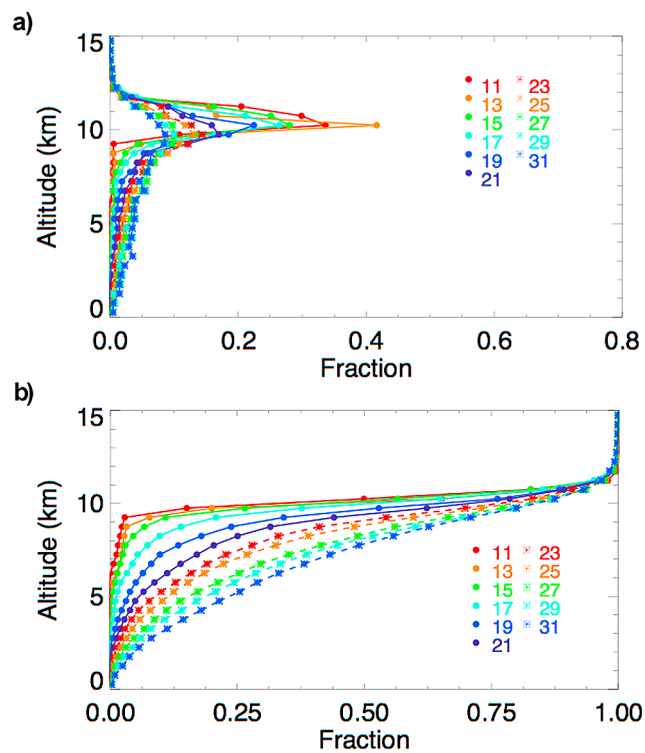

Figure 4. The mass-weighted altitude distributions of parcels initialized in the trajectory model on 11 August and run forward in time using the NASA GTM (kinematic version) through 31 August. (a) The probability distribution functions (PDFs) represent the fraction of parcels in specified vertical layers as a function of time. (b) The cumulative mass-weighted PDFs relate the fraction of parcels with altitudes below a given level as a function of time, based on the altitude distributions shown in Figure 4a.

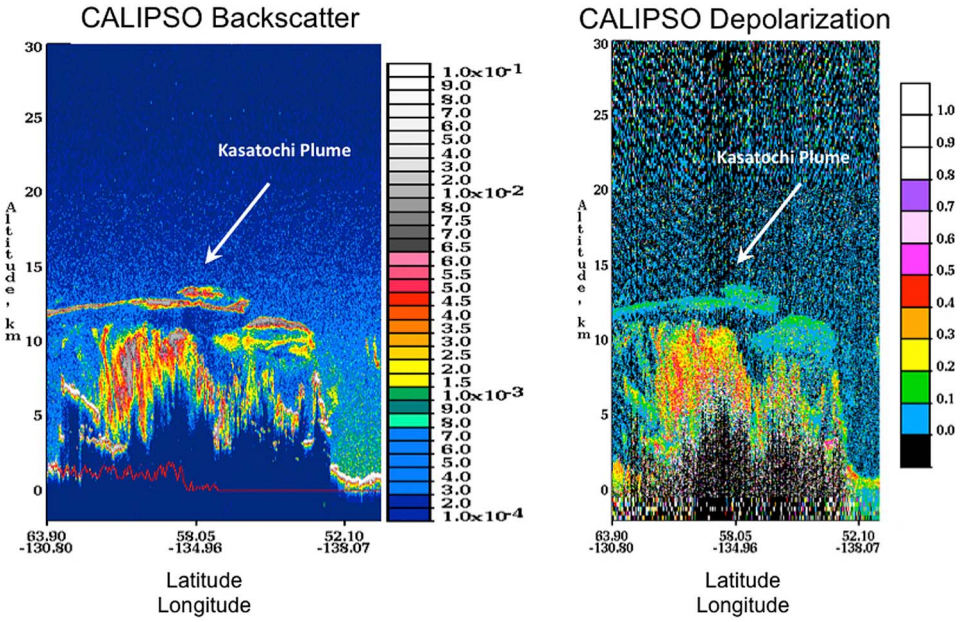

Figure 5. CALIPSO lidar browse images over northwestern Canada showing the Kasatochi cloud above the meteorological clouds. (left) The 532 total attenuated backscatter in km/sr on 12 August. Latitude and longitude are shown at the bottom. (right) The depolarization ratio; low values indicate spherical sulfate droplets rather than nonspherical ice (high depolarization ratio) confirming the volcanic origin of the plume.

7–10 days [*Sutton et al.*, 1994; *Schoeberl and Sparling*, 1995; *Morris et al.*, 1995]. Figure 4 shows the probability distribution function (PDF) of trajectory model parcel heights as a function of time every other day for the 11–31 August time period. While the peak of the PDF moves down slowly from ~10.5 to ~9.5 km over the 3 week time period of the analysis, some parcels descend rather rapidly to lower levels. The descent of these parcels can be more clearly seen

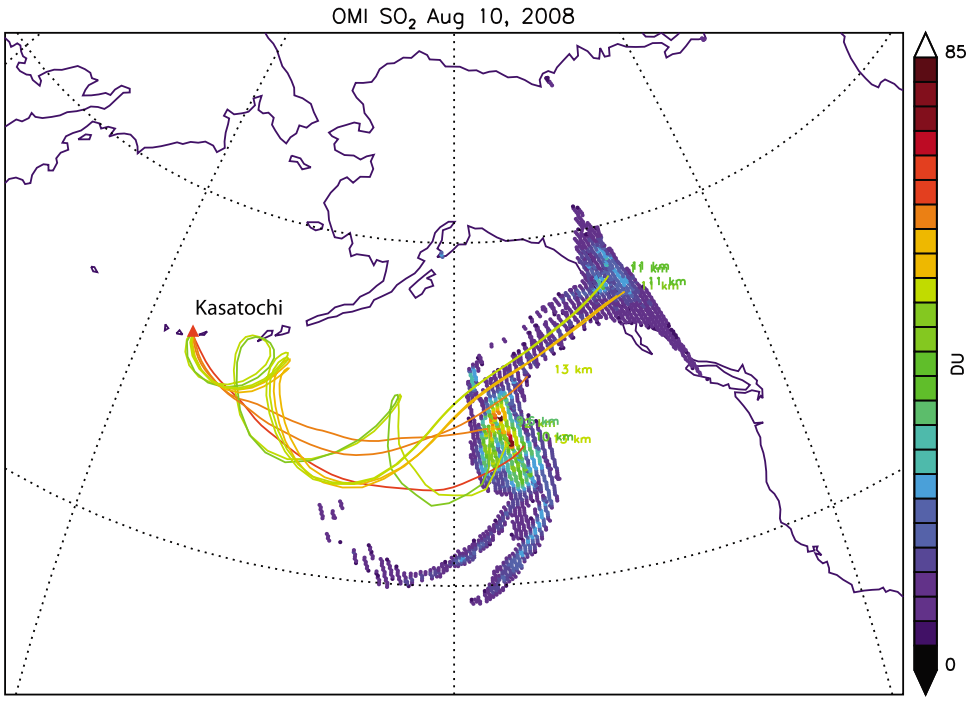

Figure 6. Individual pixels from the OMI observations on 10 August and back trajectories that come within 2.5 km of Kasatochi Island (orange triangle below label). The OMI pixels are colored based upon the SO_2 columns (DU) according to the color scale on the right.

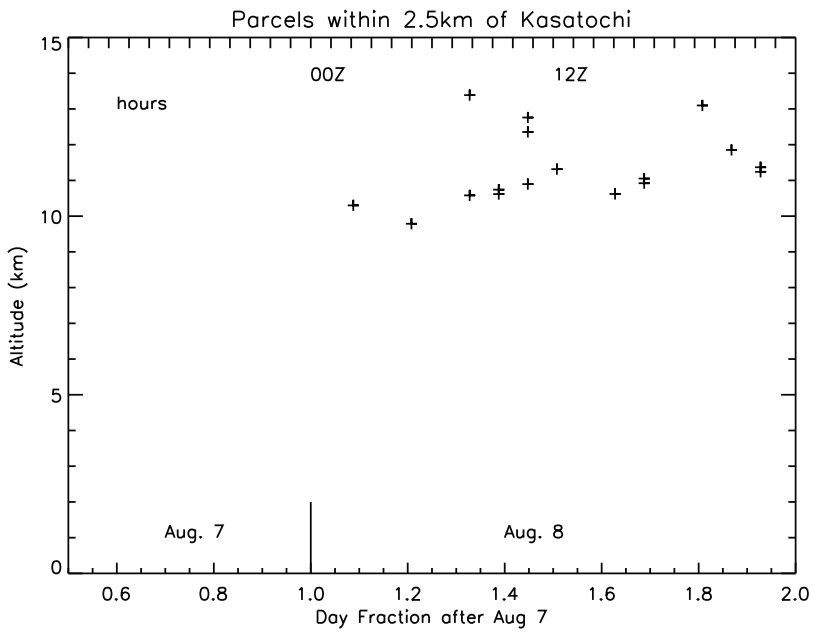

Figure 7. The arrival time (fraction of the day) to Kasatochi Island versus altitude from a back trajectory starting on 10 August 2008 (Figure 6). UT times are after 7 August with hours shown at the top. The calculation shows that the ~10 km plume initiated shortly after 0100 local time on 8 August and a ~13 km plume was initiated about 7 h later.

in the cumulative PDF plot shown in Figure 4b. Each point in the plot represents the fraction of parcels below a given altitude on a given day. The descent of the mode of the distribution is clearly visible. Table 2 provides a summary of the mean and most probable heights (i.e., the vertical 0.5 km bin with the highest number of parcels) for the cloud altitude distribution as a function of time and as indicated by the trajectory model results. This assessment is consistent with the initial eruption reports of the ash cloud extending from 10.6 km to 13.7 km (assuming that SO_2 is collocated with ash) and an isentropic assumption for SO_2 cloud dispersion. CALIPSO lidar browse images for 12 August over western Canada are shown in Figure 5. Figure 5 shows an aerosol plume between 10 and 13 km consistent with our estimates. Low values of the depolarization ratio are consistent with the dominance of spherical sulfate droplets rather than nonspherical ice or ash particles, confirming a sulfate-rich volcanic cloud composition. The GTM mean heights were used as proxies for the CMA to correct the operational OMI SO_2 retrievals (section 4.2).

3.3. Backward Trajectory Analysis of the Eruption Cloud

[17] By running the isentropic GTM backward from the 10 August 2008 volcanic cloud, we can estimate the eruption times and altitudes. In this procedure we start with parcel columns over each of the SO_2 measurement points at the measurement times, then run the trajectories backward and note those parcels that come within 2.5 km of Kasatochi Island. Figures 6 and 7 show the results of the calculation. In Figure 6 we show the back trajectory path from the SO_2 distribution of 10 August 2008 for every fifth parcel that passes within 2.5 km of Kasatochi Island. In Figure 7 we show the time and altitude of the arrival of parcels at Kasatochi. Initial SO_2 and ash cloud observations show that the eruption cloud swirled back and rotated near the volcano so we expect to have multiple arrival times occurring after the initial bursts. The multiple arrival times are also seen in Figure 7. We should only consider the earliest arrival time at each altitude. The earliest arrival time is 0130 UTC on 8 August near 10 km and a higher-altitude arrival time is about 0800 UTC on the same date. The Alaskan Volcanic Observatory reported that Kasatochi seismic activity began at 2230 UTC on 7 August with more activity at 0100–0200 UTC and 0400–0500 UTC on 8 August. The arrival time estimates are consistent with these assessments considering that plume ejection would occur after seismic activity. We also note that the eruption altitude from this calculation is consistent with our earlier estimates from the forward trajectory calculation.

4. Hemispherical SO_2 Cloud Dispersion and Observational Constraints on SO_2 Decay Rate

4.1. Dispersion Pattern Comparisons

[18] Due to its high sensitivity to stratospheric SO_2, OMI was able to track the Kasatochi SO_2 cloud for more than one month after the eruption. In comparison, IR SO_2 measurements by the IASI sensor on MetOp-A tracked the Kasatochi volcanic cloud for 29 days [*Karagulian et al.*, 2010], indicating the slightly higher sensitivity of the UV measurements. Since the OMI maps are asynoptic (i.e., measured at constant local solar time at ~1400 LST), we have generated parcel distribution maps by sampling the GTM output at times and locations of OMI overpasses. Figure 8 compares SO_2 dispersion patterns on 12–16 August as observed by OMI measurements and predicted by a kinematic GTM forward run from 11 August (described above). During this

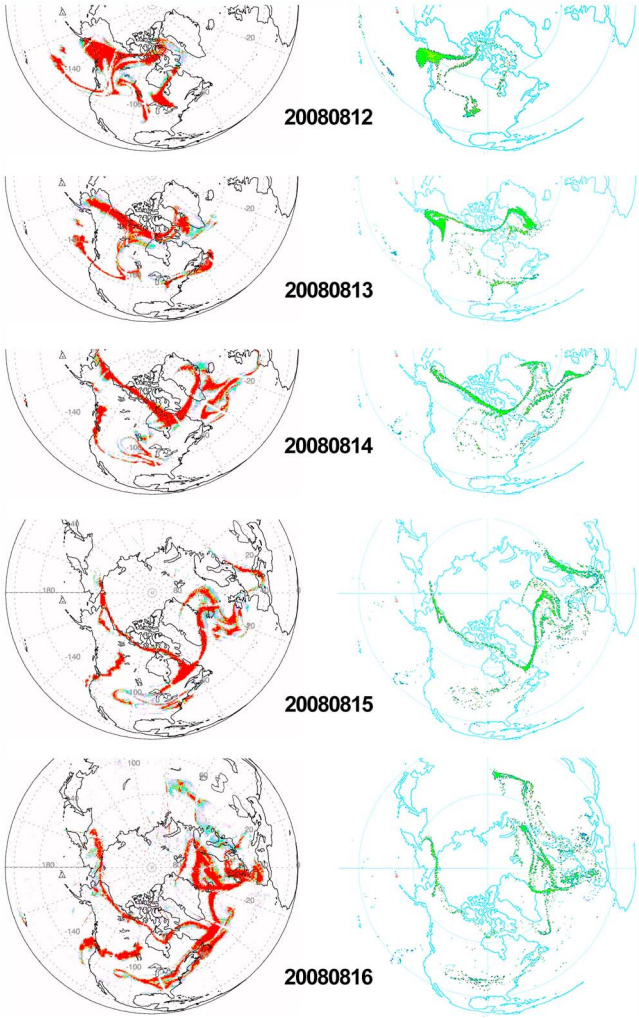

Figure 8. Kasatochi SO_2 cloud dispersion, 12–16 August 2008. (left) OMI STL data interpolated onto a regular grid and shown in a North Polar stereographic projection; the OMI SO_2 scale is from 0.2 to 1 DU to better highlight the boundaries of the Kasatochi cloud. (right) Parcel locations from the kinematic GTM forward run from 11 August 2008 to the same day with altitudes from 0 (purple) to 15 km (red), with 9–12 km in green. Note that these asynoptic maps have been produced by sampling the GTM output at times and locations of OMI overpasses.

period the eastern edge of the plume was moving quickly with jet stream winds but also meandering in a north-south direction. The leading edge quickly traversed the Atlantic on 13 August and reached the West coast of Europe on 14 August. During this day the eastern branch continued moving eastward over Europe in a wave pattern reaching as far south as the Mediterranean and as far north as the Baltic Sea. On 16 August the eastern edge was over Siberia.

[19] The western part of the northern branch drifted slowly northward over Alaska and Canada until 14 August, when the edge started moving westward, reaching eastern Siberia on 15 August. The separation of the cloud branches was intensified by the development of a deep trough in the upper troposphere over the Pacific and accompanying ridge over the western United States on 14 August. Figure 9 shows the NCEP reanalysis wind vectors and speeds at the 150 hPa level (~13 km) for 1200 UTC on 14 August. Parcels in the western edge of the cloud were carried further west, while those to the east continued eastward.

[20] By 16 August the western and eastern edges of the northern branch were both over Siberia moving toward each other, while the bulk of the plume was over the northern Atlantic. The southern branch was also moving eastward, meandering more slowly over the United States until 15 August, when the western edge reversed its course and moved back over Pacific. Despite some local differences (e.g., between the western parts of the southern branch), the features in the two maps are well correlated. The differences can be due to errors in the wind analysis or unaccounted mechanisms in the GTM (e.g., solar heating).

4.2. Observational Constraints on SO_2 Decay Rate

[21] The lifetime of SO_2 depends on its vertical profile and the concentrations of oxidants that vary with season and location. Although the global, annual averaged lifetime of SO_2 is only 1–3 days from global models [e.g., *Chin et al.*, 2000; *Barrie et al.*, 2001], SO_2 from volcanic eruptions usually has longer lifetime, especially if it is injected into the stratosphere [*Bluth et al.* 1992; *Guo et al.*, 2004; *Prata et al.*, 2007; *Eckhardt et al.*, 2008]. Correcting for the SO_2 cloud altitude evolution with time is important for the OMI SO_2 retrieval algorithm and the SO_2 chemical decay rate estimate. Here we use an estimate of the CMA derived from the trajectory model (Table 2 and Figure 4) as a proxy for the SO_2 vertical distribution, to obtain "best estimate" SO_2 mass (Table 1) by interpolating between the TRM and STL operational values. The OMI data affected by partial blocking of the OMI field of view (the so-called "row anomaly" cross-track positions 38 through 43) were interpolated using nonaffected cross-track positions. All OMI observations for a particular day were interpolated on a regular 0.1° latitude/longitude grid. Total observed daily SO_2 burdens were calculated by summing all masses in grid cells north of 30° latitude. The operational mass bias −0.05 Tg estimated on 7 August was subtracted from all the operational masses measured on 11 August to 14 September. On 8–10 August we use more accurate off-line EISF mass estimates [*Yang et al.*, 2010] (Figures 1 and 2). The combined SO_2 mass measurements are shown in Figure 10. The observed SO_2 mass increased by ~60% from ~1.1 Tg on 8 August to ~1.8 Tg late on 10 August. Early post-eruption increases in measured SO_2 burdens have been observed following several eruptions [e.g., *Rose et al.*, 2000; *Guo et al.*, 2004]. The cause remains unclear, and may differ between eruptions, but it has been attributed to gradual release of SO_2 from sublimating mixtures of ice, ash and gas, or emission of H_2S and subsequent oxidation to SO_2. Furthermore, we note that IR IASI SO_2 data did not show this SO_2 mass increase in the Kasatochi eruption cloud [*Karagulian et al.*, 2010]. Therefore, OMI measured mass on 8–10 August is likely an underestimate (e.g., due to subpixels inhomogeneity effects and/or the opacity of the initial SO_2 plume and/or ash interference [*Yang et al.*, 2010]). Operational mass estimates on 12 and 13 August are likely to be underestimated more strongly than on subsequent days. We therefore selected the time period between 14 and 31 August with the monotonic mass decline to esti-

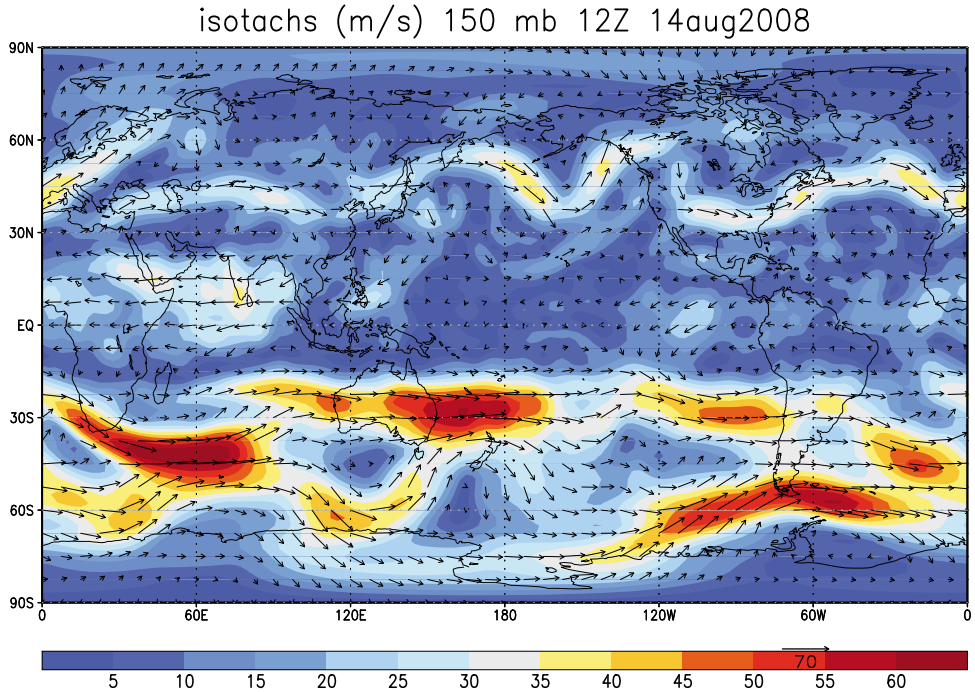

Figure 9. NCEP reanalysis wind vectors for 14 August 2008 at 1200 UT explains the separation of eastern and western parts of the OMI SO_2 plumes (see text). Image from http://nomad1.ncep.noaa.gov/.

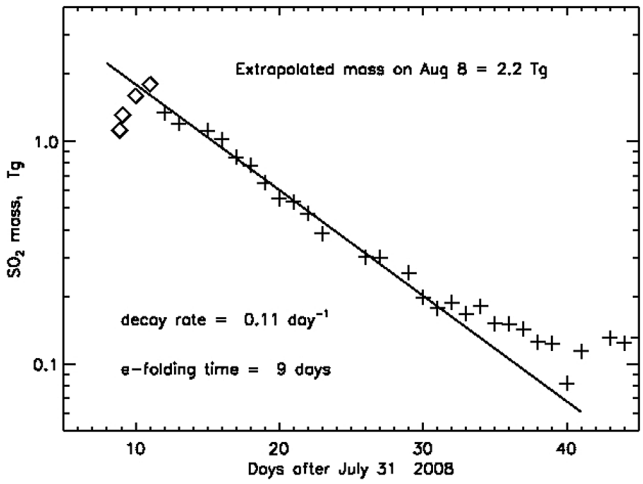

Figure 10. OMI measured altitude and row anomaly corrected SO_2 mass decay for 1 month following the Kasatochi eruption over Northern mid and high latitudes (30°N–90°N). On 8–11 August, masses are calculated using the off-line EISF algorithm (diamonds), while on 12 August to 14 September, masses are calculated using the operational LF algorithm (crosses). The largest SO_2 mass (~1.8 Tg) was measured late on 10 August using EISF algorithm (combined orbits 21663 and 21664; see Figure 2). Operational retrievals on 12 and 13 August are underestimated due to opacity of the initial plume and ash interference. On 14–31 August the mass decay can be approximated using an exponential function with the e-folding time ~9 days (solid line). Extrapolation of the exponential decay back in time yields an initial SO_2 mass of ~2.2 Tg on 8 August.

mate the chemical SO_2 loss rate (Figure 10). We assume that during this time and altitude range (i.e., 9–12 km in Figure 4) the chemical conversion of SO_2 to sulfate was the main factor compared to other removal mechanisms (e.g., dry and wet SO_2 deposition). We fit an exponential decay curve to the daily OMI SO_2 burdens (linear curve on logarithmic axis in Figure 10) to estimate a mean SO_2 lifetime of ~9 days (i.e., e-folding time). Extrapolation of the exponential decay back in time yields an initial erupted SO_2 mass of ~2.2 Tg on 8 August, twice as much as the measured mass on that day (Figure 1). We note that the monthly NH SO_2 mass remained elevated in September 2008, but the daily masses were comparable to the typical OMI day-to-day variability in NH.

[22] The estimated Kasatochi SO_2 e-folding time is significantly lower than the ~25 days reported for the 1991 Pinatubo SO_2 cloud [*Guo et al.*, 2004], but this would be consistent with the lower altitude of the Kasatochi SO_2 and its extratropical location, where the UTLS is more dynamic and sunshine duration in August is longer than in tropics. To check if the lifetime of SO_2 in the Kasatochi volcanic cloud estimated here is consistent with global chemistry-transport models, we examined a similar volcanic eruption case simulated by the GOCART model [*Chin et al.*, 2000]: the Mount Spurr (Alaska) eruption on 18 August 1992, which injected ~0.3 Tg SO_2 into the stratosphere at about 15 km. The model-estimated lifetime of the Mount Spurr SO_2 is 7–11 days, which is generally consistent with the Kasatochi SO_2 lifetime estimated based on the OMI data presented here, although a more appropriate quantitative comparison should be performed by simulating the actual Kasatochi eruption in the model (simulation is in preparation; M. Chin, personal communication, 2010). We note that the OMI e-folding time is lower than ~18 days estimated for the Kasatochi SO_2 cloud

using IASI measurements [*Karagulian et al.*, 2010]. The reasons for the discrepancies need further investigation.

5. Conclusions

[23] The ability of satellite sensors to track volcanic SO_2 clouds for extended periods promises a significant advance in our understanding of the atmospheric impacts of volcanic eruptions. OMI's high sensitivity to SO_2 provides a tool to investigate long-range transport of SO_2 clouds, validate trajectory models, and study the conversion of SO_2 to sulfate. Combining UV SO_2 measurements such as those presented here with IR SO_2 retrievals (e.g., from IASI) would provide improved temporal resolution and nighttime coverage, and permit further insights into SO_2 dispersion and chemical conversion, and into the relative sensitivity of the UV and IR measurements.

[24] The increase in measured SO_2 mass during early atmospheric residence of volcanic clouds remains enigmatic, in part due to inconsistent results from UV and IR techniques, and the reasons for this should be explored with further measurements (e.g., A-Train satellite data) and modeling work.

[25] **Acknowledgments.** Funding for this work was provided by the NASA awards NNG06GI00G (Mapping SO_2 emissions with NASA Ozone Monitoring Instrument (OMI) and GOCART model for air quality and climate science), NNH04ZYS004N (Validation of OMI L2 Sulfur Dioxide retrievals over volcanic and anthropogenic sources), and CAN NNS06AA05G (Volcanic Cloud Data for Aviation Hazards). The Dutch-Finnish-built OMI instrument is part of the NASA EOS Aura satellite payload. The OMI project is managed by NIVR and KNMI in the Netherlands. The authors would like to thank the KNMI OMI team for producing L1B radiance data and the U.S. OMI Science and Operations teams for continuing support. G.A. Morris thanks the Fulbright Scholar program and the NASA Earth Science Division for financial support while conducting this research and thanks colleagues J. Hirokawa, M. Fujiwara, and F. Hasebe in the department of Environmental Earth Science at Hokkaido University, Sapporo, Japan, where G.A. Morris conducted his research. The authors would like to thank anonymous reviewers for their important suggestions that helped improving the manuscript.

References

Ahmad, Z., P. K. Bhartia, and N. Krotkov (2004), Spectral properties of backscattered UV radiation in cloudy atmospheres, *J. Geophys. Res.*, *109*, D01201, doi:10.1029/2003JD003395.

Allen, D., and M. Schoeberl (1999), Trajectory modeling of aerosol clouds observed by TOMS, *J. Geophys. Res.*, *104*, 27,461–27,471, doi:10.1029/1999JD900763.

Barrie, L. A., et al. (2001), A comparison of large-scale atmospheric sulphate aerosol models (COSAM): Overview and highlights, *Tellus, Ser. B*, *53*, 615–645.

Barth, M., P. J. Rasch, J. T. Kiehl, C. M. Benkovitz, and S. E. Schwartz (2000), Sulfur chemistry in the National Center for Atmospheric Research Community Climate Model: Description, evaluation, features and sensitivity to aqueous chemistry, *J. Geophys. Res.*, *105*, 1387–1415, doi:10.1029/1999JD900773.

Bluth, G. J. S., S. D. Doiron, C. C. Schnetzler, A. J. Krueger, and L. S. Walter (1992), Global tracking of the SO_2 clouds from the June, 1991 Mount Pinatubo eruptions, *Geophys. Res. Lett.*, *19*, 151–154, doi:10.1029/91GL02792.

Bourassa, A. E., D. A. Degenstein, B. J. Elash, and E. J. Llewellyn (2010), Evolution of the stratospheric aerosol enhancement following the eruptions of Okmok and Kasatochi: Odin-OSIRIS measurements, *J. Geophys. Res.*, *115*, D00L03, doi:10.1029/2009JD013274.

Bovensmann, H., J. P. Burrows, M. Buchwitz, J. Frerick, S. Noël, V. V. Rozanov, K. V. Chance, and A. P. H. Goede (1999), SCIAMACHY: Mission objectives and measurement modes, *J. Atmos. Sci.*, *56*(2), 127–150, doi:10.1175/1520-0469(1999)056<0127:SMOAMM>2.0.CO;2.

Carn, S. A., A. J. Krueger, G. J. S. Bluth, S. J. Schaefer, N. A. Krotkov, I. M. Watson, and S. Datta (2003) Volcanic eruption detection by the Total Ozone Mapping Spectrometer (TOMS) instruments: A 22-year record of sulfur dioxide and ash emissions, *Spec. Publ. Geol. Soc. London*, *213*(1), 177–202.

Carn, S. A., L. L. Strow, S. de Souza-Machado, Y. Edmonds, and S. Hannon (2005), Quantifying tropospheric volcanic emissions with AIRS: The 2002 eruption of Mt. Etna (Italy), *Geophys. Res. Lett.*, *32*, L02301, doi:10.1029/2004GL021034.

Carn, S. A., A. J. Krueger, N. A. Krotkov, K. Yang, and P. F. Levelt (2007), Sulfur dioxide emissions from Peruvian copper smelters detected by the Ozone Monitoring Instrument, *Geophys. Res. Lett.*, *34*, L09801, doi:10.1029/2006GL029020.

Carn, S. A., A. J. Krueger, N. A. Krotkov, S. Arellano, and K. Yang (2008), Daily monitoring of Ecuadorian volcanic degassing from space, *J. Volcanol. Geotherm. Res.*, *176*(1), 141–150, doi:10.1016/j.jvolgeores.2008.01.029.

Carn, S. A., A. J. Krueger, N. A. Krotkov, K. Yang, and K. Evans (2009), Tracking volcanic sulfur dioxide clouds for aviation hazard mitigation, *Nat. Hazards*, *51*(2), 325–343, doi:10.1007/s11069-008-9228-4.

Chin, M., D. J. Jacob, G. M. Gardner, M. S. Foreman Fowler, P. A. Spiro, and D. L. Savoie (1996), A global three dimensional model of tropospheric sulfate, *J. Geophys. Res.*, *101*, 18,667–18,690, doi:10.1029/96JD01221.

Chin, M., R. B. Rood, S.-J. Lin, J.-F. Müller, and A. M. Thompson (2000), Atmospheric sulfur cycle in the global model GOCART: Model description and global properties, *J. Geophys. Res.*, *105*, 24,671–24,687, doi:10.1029/2000JD900384.

Clarisse, L., P. F. Coheur, A. J. Prata, D. Hurtmans, A. Razavi, T. Phulpin, J. Hadji-Lazaro, and C. Clerbaux (2008), Tracking and quantifying volcanic SO_2 with IASI, the September 2007 eruption at Jebel at Tair, *Atmos. Chem. Phys.*, *8*, 7723–7734, doi:10.5194/acp-8-7723-2008.

Clerbaux, C., P.-F. Coheur, L. Clarisse, J. Hadji-Lazaro, D. Hurtmans, S. Turquety, K. Bowman, H. Worden, and S. A. Carn (2008), Measurements of SO_2 profiles in volcanic plumes from the NASA Tropospheric Emission Spectrometer (TES), *Geophys. Res. Lett.*, *35*, L22807, doi:10.1029/2008GL035566.

Corradini, S., L. Merucci, F. Prata, and A. Piscini (2010), Volcanic ash and SO_2 in the 2008 Kasatochi and Okmok eruptions: Retrievals comparison from different IR satellite sensors, *J. Geophys. Res.*, doi:10.1029/2009JD013634, in press.

Crutzen, P. (2006), Albedo enhancement by stratospheric sulfur injections: A contribution to resolve a policy dilemma?, *Clim. Change*, *77*, 211–219, doi:10.1007/s10584-006-9101-y.

Dave, J. V. (1964), Meaning of successive iteration of the auxiliary equation of radiative transfer, *Astrophys. J.*, *140*, 1292–1303, doi:10.1086/148024.

Dean, K. G., et al. (2008), Alaska Volcano Observatory's satellite remote sensing of the Okmok and Kasatochi 2008 eruptions, *Eos Trans. AGU*, *89*(53), Fall Meet. Suppl., Abstract A53B-0265.

Eckhardt, S., A. J. Prata, P. Seibert, K. Stebel, and A. Stohl (2008), Estimation of the vertical profile of sulfur dioxide injection into the atmosphere by a volcanic eruption using satellite column measurements and inverse transport modeling, *Atmos. Chem. Phys.*, *8*, 3881–3897, doi:10.5194/acp-8-3881-2008.

Guo, S., G. J. S. Bluth, W. I. Rose, I. M. Watson, and A. J. Prata (2004), Re-evaluation of SO_2 release of the 15 June 1991 Pinatubo eruption using ultraviolet and infrared satellite sensors, *Geochem. Geophys. Geosyst.*, *5*, Q04001, doi:10.1029/2003GC000654.

Heath, D. F., A. J. Krueger, H. R. Roeder, and B. D. Henderson (1975), The Solar Backscatter Ultraviolet and Total Ozone Mapping Spectrometer (SBUV/TOMS) for Nimbus G, *Opt. Eng.*, *14*, 323–331.

Intergovernmental Panel on Climate Change (2007), *Climate Change 2007: The Physical Science Basis. Contribution of Working Group I to the Fourth Assessment. Report of the Intergovernmental Panel on Climate Change*, edited by S. Solomon et al., Cambridge Univ. Press, Cambridge, U. K.

Joiner, J., and A. P. Vasilkov (2006), First results from the OMI rotational Raman scattering cloud pressure algorithm, *IEEE Trans. Geosci. Remote Sens.*, *44*, 1272–1282, doi:10.1109/TGRS.2005.861385.

Junge, C. E., C. W. Chagnon, and J. E. Manson (1961), Stratospheric aerosols, *J. Meteorol.*, *18*, 81–108.

Karagulian, F., L. Clarisse, C. Clerbaux, A. J. Prata, D. Hurtmans, and P. F. Coheur (2010), Detection of volcanic SO_2, ash and H_2SO_4 using the IASI sounder, *J. Geophys. Res.*, *115*, D00L02, doi:10.1029/2009JD012786.

Koch, D., D. Jacob, I. Tegen, D. Rind, and M. Chin (1999), Tropospheric sulfur simulation and sulfate direct radiative forcing in the GISS GCM, *J. Geophys. Res.*, *104*, 23,799–23,822, doi:10.1029/1999JD900248.

Kristiansen, N. I., et al. (2010), Remote sensing and inverse transport modeling of the Kasatochi eruption sulfur dioxide cloud, *J. Geophys. Res.*, *115*, D00L16, doi:10.1029/2009JD013286.

Krotkov, N. A., S. A. Carn, A. J. Krueger, P. K. Bhartia, and K. Yang (2006), Band residual difference algorithm for retrieval of SO_2 from the Aura Ozone Monitoring Instrument (OMI), *IEEE Trans. Geosci. Remote Sens.*, *44*, 1259–1266, doi:10.1109/TGRS.2005.861932.

Krotkov, N. A., et al. (2008), Validation of SO_2 retrievals from the Ozone Monitoring Instrument over NE China, *J. Geophys. Res.*, *113*, D16S40, doi:10.1029/2007JD008818.

Krueger, A. J., L. S. Walter, P. K. Bhartia, C. C. Schnetzler, N. A. Krotkov, I. Sprod, and G. Bluth (1995), Volcanic sulfur dioxide measurements from the Total Ozone Mapping Spectrometer (TOMS) instruments, *J. Geophys. Res.*, *100*, 14,057–14,076, doi:10.1029/95JD01222.

Krueger, A. J., S. J. Schaefer, N. A. Krotkov, I. Sprod, G. J. S. Bluth, and S. Barker (2000), Ultraviolet remote sensing of volcanic emissions, in *Remote Sensing of Active Volcanism*, *Geophys. Monogr. Ser.*, vol. 116, edited by P. J. Mouginis-Mark, J. A. Crisp, and J. H. Fink, pp. 25–42, AGU, Washington, D. C.

Krueger, A. J., K. Yang, and N. Krotkov (2009a), Enhanced monitoring of sulfur dioxide sources with hyperspectral UV sensors, *Proc. SPIE Int. Soc. Opt. Eng.*, *7475*, 74750Y.

Krueger, A., N. Krotkov, K. Yang, S. Carn, G. Vicente, and W. Schroeder (2009b), Applications of satellite-based sulfur dioxide monitoring, *IEEE J. Selected Topics Appl. Earth Obs. Remote Sens.*, *2*(N4), 293–298, doi:10.1109/JSTARS.2009.2037334.

Lee, C., A. Richter, M. Weber, and J. P. Burrows (2008), SO_2 retrieval from SCIAMACHY using the weighting function DOAS (WFDOAS) technique: Comparison with standard DOAS retrieval, *Atmos. Chem. Phys.*, *8*, 6137–6145, doi:10.5194/acp-8-6137-2008.

Levelt, P. F., et al. (2006), The Ozone Monitoring Instrument, *IEEE Trans. Geosci. Remote Sens.*, *44*(5), 1093–1101, doi:10.1109/TGRS.2006.872333.

McKeen, S. A., S. C. Liu, and C. S. Kiang (1984), On the chemistry of stratospheric SO_2 from volcanic eruptions, *J. Geophys. Res.*, *89*, 4873–4881, doi:10.1029/JD089iD03p04873.

Morris, G. A., et al. (1995), Trajectory mapping and applications to data from the Upper Atmosphere Research Satellite, *J. Geophys. Res.*, *100*, 16,491–16,505, doi:10.1029/95JD01072.

Prata, A. J., and C. Bernardo (2007), Retrieval of volcanic SO_2 column abundance from Atmospheric Infrared Sounder data, *J. Geophys. Res.*, *112*, D20204, doi:10.1029/2006JD007955.

Prata, A. J., and J. Kerkmann (2007), Simultaneous retrieval of volcanic ash and SO_2 using MSG-SEVIRI measurements, *Geophys. Res. Lett.*, *34*, L05813, doi:10.1029/2006GL028691.

Prata, A. J., S. Self, W. I. Rose, and D. M. O'Brien (2003), Global, long-term sulphur dioxide measurements from TOVS data: A new tool for studying explosive volcanism and climate, in *Volcanism and the Earth's Atmosphere*, *Geophys. Monogr. Ser.*, vol. 139, edited by A. Robock and C. Oppenheimer, pp. 75–92, AGU, Washington, D. C.

Prata, A. J., S. A. Carn, A. Stohl, and J. Kerkmann (2007), Long range transport and fate of a stratospheric volcanic cloud from Soufrière Hills volcano, Montserrat, *Atmos. Chem. Phys.*, *7*, 5093–5103, doi:10.5194/acp-7-5093-2007.

Prata, A. J., G. Gangale, L. Clarisse, and F. Karagulian (2010), Ash and sulphur dioxide in the 2008 eruptions of Okmok and Kasatochi: Insights from high spectral resolution satellite measurements, *J. Geophys. Res.*, *115*, D00L18, doi:10.1029/2009JD013556.

Richter, A., F. Wittrock, and J. P. Burrows (2006), SO_2 measurements with SCIAMACHY, in *Proceedings of the First Conference on Atmospheric Science* [CD-ROM], *ESA Publ. SP-628*, ESA, Frascati, Italy.

Richter, A., F. Wittrock, A. Schönhardt, and J. P. Burrows (2009), Quantifying volcanic SO_2 emissions using GOME-2 measurements, *Geophys. Res. Abstr.*, *11*, Abstract EGU2009-7679.

Robock, A. (2000), Volcanic eruptions and climate, *Rev. Geophys.*, *38*, 191–219, doi:10.1029/1998RG000054.

Robock, A., L. Oman, and G. Stenchikov (2008), Regional climate responses to geoengineering with tropical and Arctic SO_2 injections, *J. Geophys. Res.*, *113*, D16101, doi:10.1029/2008JD010050.

Rose, W. I., G. J. S. Bluth, and G. G. J. Ernst (2000), Integrating retrievals of volcanic cloud characteristics from satellite remote sensors: A summary, *Philos. Trans. R. Soc. Ser. A*, *358*, 1585–1606, doi:10.1098/rsta.2000.0605.

Rosen, J. M. (1971), The boiling point of stratospheric aerosols, *J. Appl. Meteorol.*, *10*, 1044–1045, doi:10.1175/1520-0450(1971)010<1044:TBPOSA>2.0.CO;2.

Russell, P. B., et al. (1996), Global to microscale evolution of the Pinatubo volcanic aerosol derived from diverse measurements and analyses, *J. Geophys. Res.*, *101*, 18,745–18,763, doi:10.1029/96JD01162.

Schoeberl, M. R., and L. Sparling (1995), Trajectory Modeling, in *Diagnostic Tools in Atmospheric Physics, Proc. Int. School Phys. "Enrico Fermi,"* vol. 124, edited by G. Fiocco and G. Visconti, pp. 289–306, Soc. Ital. di Fis., Bologna, Italy.

Schoeberl, M. R., S. Doiron, L. R. Lait, P. A. Newman, and A. J. Krueger (1993), A simulation of the Cerro Hudson SO_2 cloud, *J. Geophys. Res.*, *98*, 2949–2955, doi:10.1029/92JD02517.

Schoeberl, M. R., et al. (2006), Overview of the EOS Aura Mission, *IEEE Trans. Geosci. Remote Sens.*, *44*(5), 1066–1074, doi:10.1109/TGRS.2005.861950.

Sioris, C. E., C. D. Boone, P. F. Bernath, J. Zou, C. T. McElroy, and C. A. McLinden (2010), Atmospheric Chemistry Experiment (ACE) observations of aerosol in the upper stratosphere and lower stratosphere from the Kasatochi volcanic eruption, *J. Geophys. Res.*, *115*, D00L14, doi:10.1029/2009JD013469.

Solomon, S. (1999), Stratospheric ozone depletion: A review of concepts and history, *Rev. Geophys.*, *37*, 275–316, doi:10.1029/1999RG900008.

Spinei, E., S. A. Carn, N. A. Krotkov, G. H. Mount, K. Yang, and A. Krueger (2010), Validation of ozone monitoring instrument SO_2 measurements in the Okmok volcanic cloud over Pullman, WA, July 2008, *J. Geophys. Res.*, *115*, D00L08, doi:10.1029/2009JD013492.

Stohl, A., M. Hittenberger, and G. Wotawa (1998), Validation of the Lagrangian particle dispersion model FLEXPART against large scale tracer experiment data, *Atmos. Environ.*, *32*, 4245–4264, doi:10.1016/S1352-2310(98)00184-8.

Sutton, R. T., H. Maclean, R. Swinbank, A. O'Neill, and F. W. Taylor (1994), High-resolution stratospheric tracer fields estimated from satellite observations using Lagrangian trajectory calculations, *J. Atmos. Sci.*, *51*(20), 2995–3005, doi:10.1175/1520-0469(1994)051<2995:HRSTFE>2.0.CO;2.

Twomey, S. (1977), The influence of pollution on the shortwave albedo of clouds, *J. Atmos. Sci.*, *34*(7), 1149–1154, doi:10.1175/1520-0469(1977)034<1149:TIOPOT>2.0.CO;2.

Watson, I. M., V. J. Realmuto, W. I. Rose, A. J. Prata, G. J. S. Bluth, Y. Gu, C. E. Bader, and T. Yu (2004), Thermal infrared remote sensing of volcanic emissions using the moderate resolution imaging spectroradiometer, *J. Volcanol. Geotherm. Res.*, *135*(1–2), 75–89, doi:10.1016/j.jvolgeores.2003.12.017.

Waythomas, C. F., W. E. Scott, S. G. Prejean, D. J. Schneider, P. Izbekov, and C. J. Nye (2010), The 7–8 August 2008 eruption of Kasatochi Volcano, central Aleutian Islands, Alaska, *J. Geophys. Res.*, *115*, B00B06, doi:10.1029/2010JB007437.

Wigley, T. M. (2006), A combined mitigation/geoengineering approach to climate stabilization, *Science*, *314*, 452–454, doi:10.1126/science.1131728.

Yang, K., N. A. Krotkov, A. J. Krueger, S. A. Carn, P. K. Bhartia, and P. F. Levelt (2007), Retrieval of large volcanic SO_2 columns from the Aura Ozone Monitoring Instrument: Comparison and limitations, *J. Geophys. Res.*, *112*, D24S43, doi:10.1029/2007JD008825.

Yang, K., N. A. Krotkov, A. J. Krueger, S. A. Carn, P. K. Bhartia, and P. F. Levelt (2009), Improving retrieval of volcanic sulfur dioxide from backscattered UV satellite observations, *Geophys. Res. Lett.*, *36*, L03102, doi:10.1029/2008GL036036.

Yang, K., X. Liu, P. K. Bhartia, N. Krotkov, S. Carn, E. Hughes, A. Krueger, R. Spurr, and S. Trahan (2010), Direct retrieval of sulfur dioxide amount and altitude from spaceborne hyperspectral UV measurements: Theory and application, *J. Geophys. Res.*, *115*, D00L09, doi:10.1029/2010JD013982.

S. Carn, Department of Geological and Mining Engineering and Sciences, Michigan Technological University, Houghton, MI 49931, USA.

N. A. Krotkov, NASA Goddard Space Flight Center, MS 613.3, Greenbelt, MD 20771, USA. (nickolay.a.krotkov@nasa.gov)

G. A. Morris, Department of Physics and Astronomy, Valparaiso University, Valparaiso, IN 46383, USA.

M. R. Schoeberl, Science and Technology Corporation, 10005 Old Columbia Rd., Ste. M-150, Columbia, MD 21046, USA.

K. Yang, Goddard Earth Sciences and Technology Center, University of Maryland Baltimore County, Baltimore, MD 21228, USA.